

Influence of Nanopillar Arrays on Fibroblast Motility, Adhesion, and Migration Mechanisms

Kai S. Beckwith, Sindre Ullmann, Jakob Vinje, and Pawel Sikorski*


Surfaces decorated with high aspect ratio nanostructures are a promising tool to study cellular processes and design novel devices to control cellular behavior. However, little is known about the dynamics of cellular phenomenon such as adhesion, spreading, and migration on such surfaces. In particular, how these are influenced by the surface properties. In this work, fibroblast behavior is investigated on regular arrays of 1 μm high polymer nanopillars with varying pillar to pillar distance. Embryonic mouse fibroblasts (NIH-3T3) spread on all arrays, and on contact with the substrate engulf nanopillars independently of the array pitch. As the cells start to spread, different behavior is observed. On dense arrays which have a pitch equal or below 1 μm , cells are suspended on top of the nanopillars, making only sporadic contact with the glass support. Cells stay attached to the glass support and fully engulf nanopillars during spreading and migration on the sparse arrays which have a pitch of 2 μm and above. These alternate states have a profound effect on cell migration rates. Dynamic F-actin puncta colocalize with nanopillars during cell spreading and migration. Strong membrane association with engulfed nanopillars might explain the reduced migration rates on sparse arrays.

1. Introduction

Cells on vertically aligned high aspect ratio nanostructures (HARNs) has been an area of great research interest in recent years.^[1] Examples include surface-based delivery of molecules to cells aided by the nanostructures,^[2–9] intracellular electrical measurements,^[10–12] capture of circulating tumor cells,^[13–15] induction of stem cell phenotypes,^[16,17] intracellular sensing,^[18–20] site-specific cellular imaging,^[11,21,22] stimulation

Dr. K. S. Beckwith, S. Ullmann
Centre of Molecular Inflammation Research
Department of Molecular and Clinical Medicine
Faculty of Medicine and Health Sciences
Norwegian University of Science and Technology
(NTNU) 7491 Trondheim, Norway

J. Vinje, Prof. P. Sikorski
Department of Physics
Norwegian University of Science and Technology (NTNU)
7491 Trondheim, Norway
E-mail: pawel.sikorski@ntnu.no

 The ORCID identification number(s) for the author(s) of this article can be found under <https://doi.org/10.1002/sml.201902514>.

© 2019 The Authors. Published by WILEY-VCH Verlag GmbH & Co. KGaA, Weinheim. This is an open access article under the terms of the Creative Commons Attribution License, which permits use, distribution and reproduction in any medium, provided the original work is properly cited.

DOI: 10.1002/sml.201902514

of cell mechanotransduction machinery^[23] or controlling the geometry of in vitro neuronal networks.^[24]

Recently arrays of SU-8 nanopillars were employed to demonstrate that in contrast to previous measurements the highest cell traction forces are not generated at the cell periphery, but instead are associated with perinuclear adhesions.^[25] In a different report an ultraflexible GaAs nanowire array was used as a nanomechanical biosensor to probe cell-induced forces by living cells with a resolution of 50 piconewton.^[26] An attempt to control the geometry of in vitro cultivated neuronal cells revealed that the cytoskeleton dynamics at the axon shaft in primary hippocampal rat neurons were changed when cultivated on hard poly(dimethylsiloxane) nanopillar arrays, which in turn lead to enhanced formation of axon collateral branches.^[27] An example of in vivo application is provided by Tang et al. who apply vertically oriented Au–TiO₂

nanowire arrays as artificial photoreceptors which restore functional and behavioral light sensitivity in blind mice.^[28]

Despite the range of applications, there is still much unknown about how cells are influenced by HARNs. High viability and reduced spreading area of adherent cells is often reported.^[29] Arrays of nanowires have been shown to inhibit fibroblast migration with longer nanowires having a stronger effect,^[30] while small patches of nanopillars inhibited neuronal cell migration.^[31] Reduced spreading of cells on HARN arrays has been reported,^[16,32] as well as altered expression of genes related to the cytoskeleton and cell adhesion.^[33,34] It has also been demonstrated that the cell membrane is able to wrap tightly over HARNs while maintaining membrane integrity.^[35–37] Careful investigations of the membrane integrity in cardiomyocyte-like HL-1 cells and Human embryonic kidney cells (HEK 293) on a variety of nanostructures by Dipalo et al. showed that vertical nanostructures can spontaneously penetrate the cellular membrane only in rare cases and under specific conditions.^[35]

Local membrane curvature can act as a biochemical signal for endocytic proteins, and HARNs which induced sites of positive membrane curvature were found to be hot spots for clathrin-mediated endocytosis (CME), as determined by preferential accumulation of CME-related proteins at these sites.^[38,39] Nanopillars were also applied for controlled probing of nuclear mechanical properties.^[40] In that report, the mechanism of nuclear deformation was linked to adhesive actin patches associating with the nanopillars, pulling the nucleus down, as well

as a stress-fiber linked actin “tent” at the apical membrane exerting a downward force. Meanwhile focal adhesions on nanowire arrays have been shown to be somewhat upregulated in one report,^[41] however they localized mainly on the substrate between nanowires.

Depending on the HARN array pitch, two distinct cell adhesion states have been reported: cells can be suspended on top of the nanostructures in a “bed of nails” effect, or adhere to the substrate with the HARNs protruding into, and even through the cell body with the cell plasma membrane wrapped around nanostructures.^[16,29,42] We have previously shown that on 1 μm high nanopillar arrays, interim and dynamic states are also possible, where only smaller regions of the cell maintains substrate contact at a given time.^[32] The critical array pitch for each state has been theoretically indicated to depend on nanostructure (NS) geometry, and has been experimentally shown to depend on surface chemistry, which influences cell-substrate adhesion.^[42] The nomenclature defining HARN densities presented by Bonde et al. splits densities into three ranges: high density ≥ 30 NS/100 μm^2 , 1 < medium density < 30 NS/100 μm^2 , and low density ≤ 1 NS/100 μm^2 .^[29]

Carefully selected nanostructures have the potential to facilitate targeting and high throughput studies of certain molecular events in living cells. This can for example include endocytosis, formation of adhesion points, receptor clustering, dynamic of the cytoskeleton, or cell membrane mechanics. Much is still unknown regarding which structures are needed to activate certain biochemical signals and how these could be used in both screening and fundamental cell biology research. This is because most reported studies are performed on static, fixed cells. Substrates used for HARN are typically opaque, limiting possibilities of detailed dynamic studies of cell-nanostructure interactions with optical microscopy. Throughput of employed nanofabrication processes is often a significant bottleneck as well, as cell studies require many samples with relatively large area ($\approx \text{cm}^2$).

To better understand the cell responses to HARNs and how they might be manipulated, we investigate the dynamics of embryonic mouse fibroblast (NIH-3T3) adhesion, spreading and migration on arrays of high aspect ratio polymer nanopillars as a function of array pitch. The NIH-3T3 fibroblast are stably transfected with LifeAct-mNeonGreen,^[43] and PH-PLCd1-mScarlet^[44,45] allowing for live visualization of filamentous actin (F-actin) and the plasma membrane respectively. LifeAct is a 17-amino-acid long peptide that stains F-actin structures in eukaryotic cells and tissues.^[43] The actin cytoskeleton is an essential part of cells motility apparatus producing pushing forces for protrusions through energy gained from actin polymerization, as reviewed elsewhere.^[46] The structural polarity of actin filaments generates a directional pushing force upon polymerization into F-actin,^[47] due to that the barbed end (“plus end”) polymerizes faster than the pointed end (“minus end”).^[48]

We employ nanopillar arrays fabricated with electron beam lithography (EBL) directly on microscopy-grade glass. The nanopillars are made from the stable, stiff and cell compatible polymer SU-8.^[49,50] Furthermore we and others, have previously demonstrated that substrates decorated with surface bound HARNs do not affect cell viability across HARN densities,^[4,5,32,33,41] also reviewed in Bonde et al.^[29] We show that lamellipodium-induced membrane and cytoskeleton

configuration around nanopillars strongly depends on pillar spacing on the substrate (array pitch). Lamellipodium-induced cell adhesion occurs immediately once the cells encounter the nanopillars during settling. Subsequent spreading and resulting cell adherence states are strongly influenced by the nanopillar pitch. During cell migration, cells form highly dynamic F-actin bundles at nanopillar sites, while focal adhesions form on the substrate between the nanopillars. Cell migration is reduced on sparse nanopillar arrays, but unchanged on denser arrays displaying the “bed of nails” effect. Our detailed dynamic studies shed new light on the range of mechanobiological interactions that may occur between cells and nanostructures.

2. Results

2.1. Nanopillar Arrays

Nanopillar arrays were fabricated similar to our previously described approach,^[32] but with a 100 keV Elionix GLS-100 EBL system, which allows production of nanopillars with a more uniform tip/base diameter and with a much higher fabrication throughput (pattern writing speed >1 $\text{mm}^2 \text{min}^{-1}$). **Figure 1** shows examples of fabricated nanopillar arrays illustrating uniform and reproducible nanopillar geometry. Nanopillar tip diameter is in the range of 90 nm, and the diameter at the base is 130 nm for the 1 μm high nanopillars used in this study. For fluorescence imaging, the nanopillars could be doped with a fluorescent dye such as Oxazine-170 (far-red excitation and emission), shown in **Figure 1C**. Hexagonal arrays of nanopillars with pitches of 0.75–10 μm were made in mm^2 areas on glass coverslips mounted into polystyrene cell culture dishes (35 mm dishes or 96 well plates). This setup for nanopillar arrays is ideal for high resolution microscopy of the interface between cells and nanostructures due to the possibility of imaging live cells in an inverted optical microscope with a low working distance, high numerical aperture objective.

We will refer to nanopillar arrays with pitch ≤ 1 μm as dense and ≥ 2 μm as sparse. This corresponds to densities ≥ 115 NS/100 μm^2 and ≤ 28.6 NS/100 μm^2 , respectively. With reference to the nomenclature previously presented from Bonde et al. this places the nanopillar arrays with pitch ≤ 1 μm in the high density range (1 μm array pitch = 115 NS/100 μm^2 , 0.75 μm array pitch = 205 NS/100 μm^2). Furthermore nanopillar arrays with pitch ≥ 2 μm are all in the medium density range (2, 5, and 10 μm array pitch correspond to 28.6, 4.6, and 1.15 NS/100 μm^2 , respectively).

Prior to investigating cell migration and attachment on the nanopillar arrays, we verified that cell membrane and actin filaments could be visualized using the employed labeling strategy. **Figure 2A,B** shows micrographs of NIH-3T3 fibroblasts cultured on a glass substrate for 24h. PH-PLCd1-mScarlet label (orange) was concentrated on the plasma membrane, as well as on a few intracellular vesicles (**Figure 2A**). LifeAct-mNeonGreen signal (green) clearly visualized cytoskeletal F-actin architecture (**Figure 2B**).

Membrane and actin configurations for NIH-3T3 fibroblasts expressing LifeAct-mNeonGreen (green) and PH-PLCd1-mScarlet (orange) on dense and sparse nanopillar arrays are

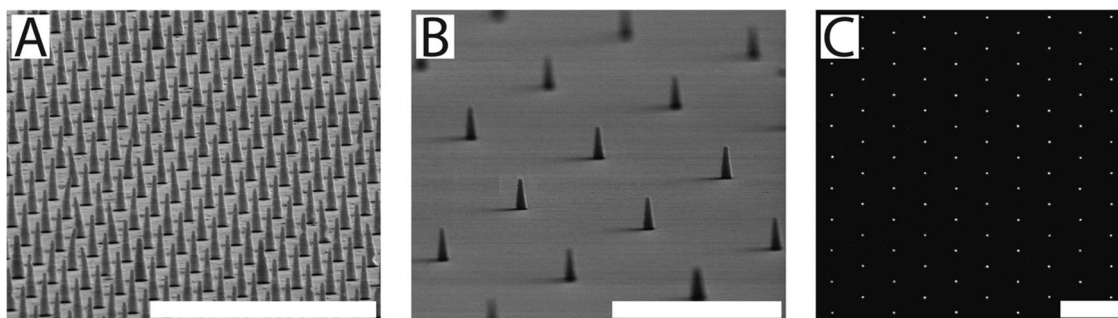


Figure 1. Overview of the nanopillar arrays used in this work. Tilted scanning electron micrographs of hexagonal SU-8 nanopillar arrays on glass cover slips with A) 0.75 μm and B) 5 μm pitch. C) Confocal laser scanning microscopy image of 5 μm pitch nanopillars array made from SU-8 doped with 100 $\mu\text{g mL}^{-1}$ oxazine-170 dye. Scale bars A,B) 5 μm and C) 10 μm .

presented in Figure 2C,F. Single confocal plane images at $\approx 50\%$ pillar height (500 nm), as well as xz and yz projections from corresponding z -stacks (side panels), are presented

with fluorescent signal from the SU-8 nanopillars doped with Oxazine-170 shown in blue. The confocal plane at 50% of the pillar height was chosen because the contrast between dense

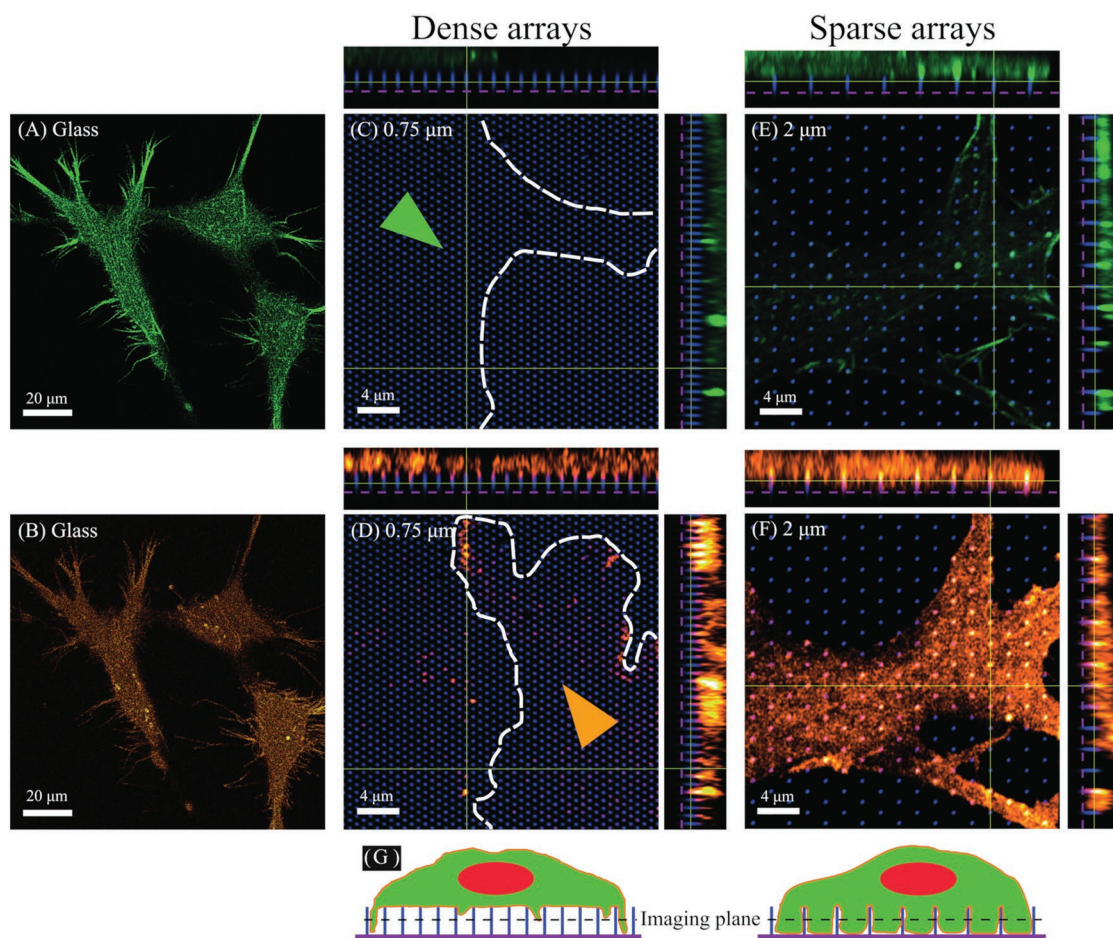


Figure 2. Initial characterization of NIH-3T3 fibroblasts expressing LifeAct-mNeonGreen (green) and PH-PLCd1-mScarlet (orange) localizing to F-actin and plasma membrane respectively. Single plane confocal images acquired right above the glass substrate of the A) F-actin signal and B) membrane signal recorded for cells cultured on a glass substrate for 24 h. High resolution Airyscan z -stacks with orthogonal projections of cells on arrays with a pitch of C,D) 0.75 μm and E,F) 2 μm . Central, single plane images are taken at 50% of the pillar height. Dashed magenta lines in the side panels indicate the approximate location of the coverslip. C) Green arrow and D) orange arrow indicate position of two cell bodies enclosed by white dashed lines. For the dense array C) no F-actin and D) only fragmented membrane signal are observed at the 50% height (500 nm), indicating that the cell body is suspended on the top of the array. For the sparse arrays E) F-actin and F) membrane signals are observed for the whole cell, indicating that cells are in contact with the glass substrate and wrap around nanopillars. For the sparse arrays, membrane signal colocalizes with the signal from the nanopillars (pink color overlay). Images presented are representative of $n \geq 50$ cells for both dense and sparse arrays. G) Schematic of the two states observed on dense and sparse arrays.

and sparse arrays was clearly visible at this height. As the airyscan technique provides an improved axial resolution of 350 nm, membrane and F-actin located on the top of the array will only give a very weak fluorescent signal if the images are taken at 50% height. On the contrary, cells wrapping around the pillars and reaching toward the glass will give a strong signal. Membrane signal colocalizes with the pillar signal along the pillar length for sparse arrays, seen as a pink color in both xy , xz , and yz images (Figure 2F). As previously described, the signal enhancement in the membrane channel is due to the membrane wrapping around the nanopillars.^[32] At some nanopillar locations F-actin signal was also clearly enhanced (F-actin puncta visible as bright green color in the side panels, Figure 2E). For dense arrays, the plasma membrane was associated with nanopillars at the top of the pillar surface (Figure 2D, side panels). Membrane wrapped around nanopillars at the cell periphery indicates that cells made contact with the glass support, seen in the side panels of Figure 2D, an observation

supported further by total internal reflection fluorescence (TIRF) microscopy in Figure 3. On dense arrays, F-actin signal was only observed above the top of the nanopillar array, again indicating that most of the cell body is suspended on the top of dense nanopillar arrays (Figure 2C, side panels).

These results were corroborated by live-cell TIRF microscopy using the fluorescence signal from the cell membrane of NIH-3T3 fibroblasts expressing PH-PLCd1-mScarlet (Figure 3). Cells on 0.75 and 1 μm pitch nanopillar arrays (Figure 3A,B) had only small patches of cell membrane visible in the TIRF mode, while a strong signal was observed in the EPI mode. These patches were located at the cell periphery and indicate that the cell membrane was in contact with the substrate only in these areas. The rest of the cell body was suspended on top of the nanopillar array. For sparse arrays, illustrated here by TIRF data for nanopillar spacing of 2 μm , a larger area of the cell membrane was in contact with the glass substrate underneath the cell body, indicating that the cell was

TIRF Membrane - EPI membrane - Nanopillars

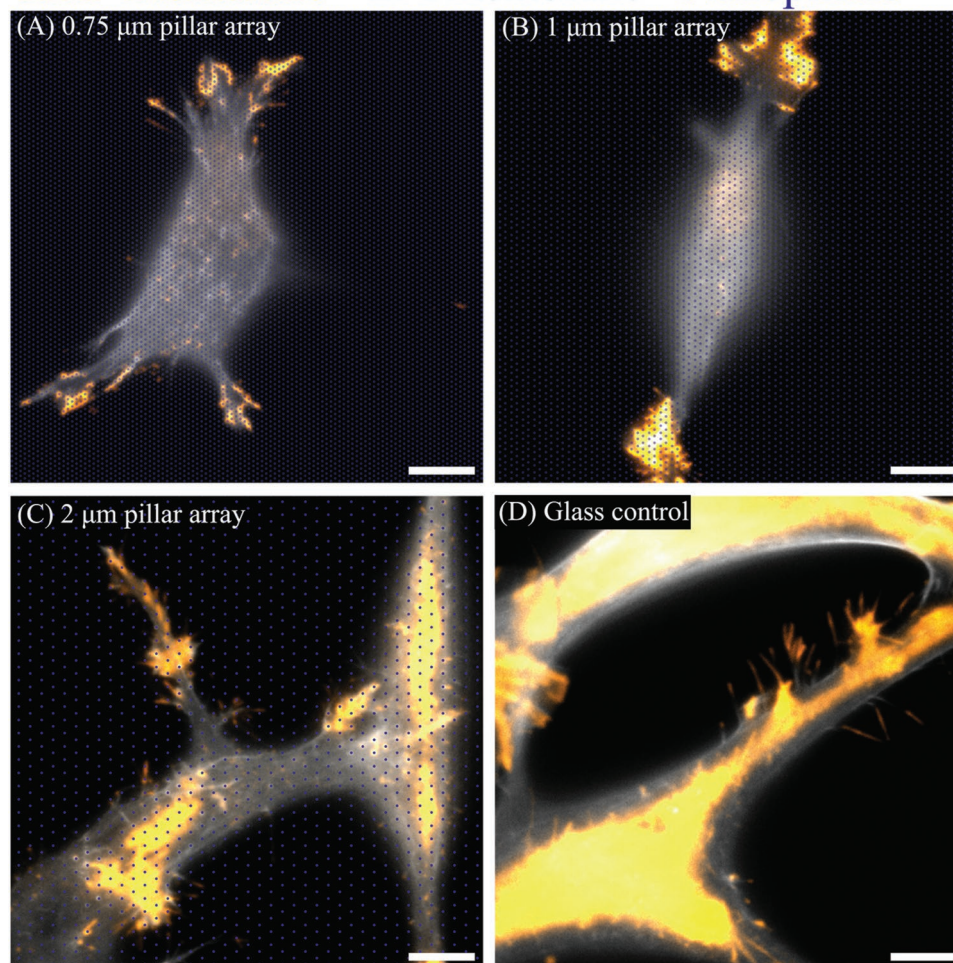


Figure 3. TIRF Data for NIH-3T3 fibroblasts 24 h after seeding expressing PH-PLCd1-mScarlet localizing to the plasma membrane. No TIRF signal from the cell bodies for cells on nanopillars with A) 0.75 μm and B) 1 μm spacing indicate that the membrane is not in contact with the glass except at the periphery of the cells. The contact underneath the cell body is partially re-established on surfaces with larger nanopillar spacing, e.g., C) 2 μm pitch arrays. Cells seeded on D) glass had high signal from the membrane both in EPI fluorescence and in TIRF modes, indicating that the membrane is in contact with the glass surface. Scale bars 10 μm . Images presented representative of $n \geq 5$ cells for all conditions.

wrapping around the nanopillars to a larger extent (Figure 3C). For the glass control (Figure 3D), strong fluorescent signal was observed both in widefield fluorescence mode and in TIRF mode, indicating that the cell membrane was in immediate proximity to the glass substrate.

2.2. Fibroblast Spreading on Nanopillar Arrays

In addition to describing cell conformation on various nanopillar arrays, we have used live cell microscopy to study the dynamics of initial cell attachment and settling of NIH-3T3 cells (Figure 4). Membrane and F-actin dynamics are further presented in Movies S01–S03 (Supporting Information). Control glass areas at the edge of the nanopillar arrays are shown to allow direct comparison of cell behavior on these two surfaces. Cells were detached from culture dishes by trypsin-ethylenediaminetetraacetic acid (EDTA) treatment and seeded onto nanopillar samples positioned on the microscope and imaged for $t > 3$ h.

On dense arrays cells were able to engulf nanopillars and explored the glass surface upon initial contact (indicated cells in Figure 4A). However, as soon as cells started to spread this contact was lost and the cells stayed on the top of the arrays,

and only explored the glass surface at the cell periphery (Figure 4A and Movie S01, Supporting Information). This was also revealed in the traces of membrane signal at individual nanopillars. In traces 1, 2, and 4 the membrane signal transiently returned when the edge of cells move across the traced nanopillar. In trace 3 the cell migrated onto the dense nanopillar array and the leading edge reached down to the glass surface, but when more of the cell body moved onto the array the cell pulled up on top of the nanopillars (see also Movie S01 in the Supporting Information).

On sparse arrays nanopillars were also engulfed early in the settling process (Figure 4B and Movies S02 and S03, Supporting Information). However, in contrast to the dense arrays, the nanopillar engulfment was stable during cell spreading and migration. For nanopillars engulfed by cells migrating on the array (trace 8), as well as for nanopillars engulfed by cells migrating onto the nanopillar array (trace 9), the membrane signal was stable after the initial engulfment. F-actin and membrane signals were enhanced at the location of the nanopillars through the mechanism described above already after the initial contact with the surface. From the presented traces it is clear that cells stay in contact with the glass coverslip after initial contact both on (traces 6 and 7) and off nanopillar arrays (trace 10).

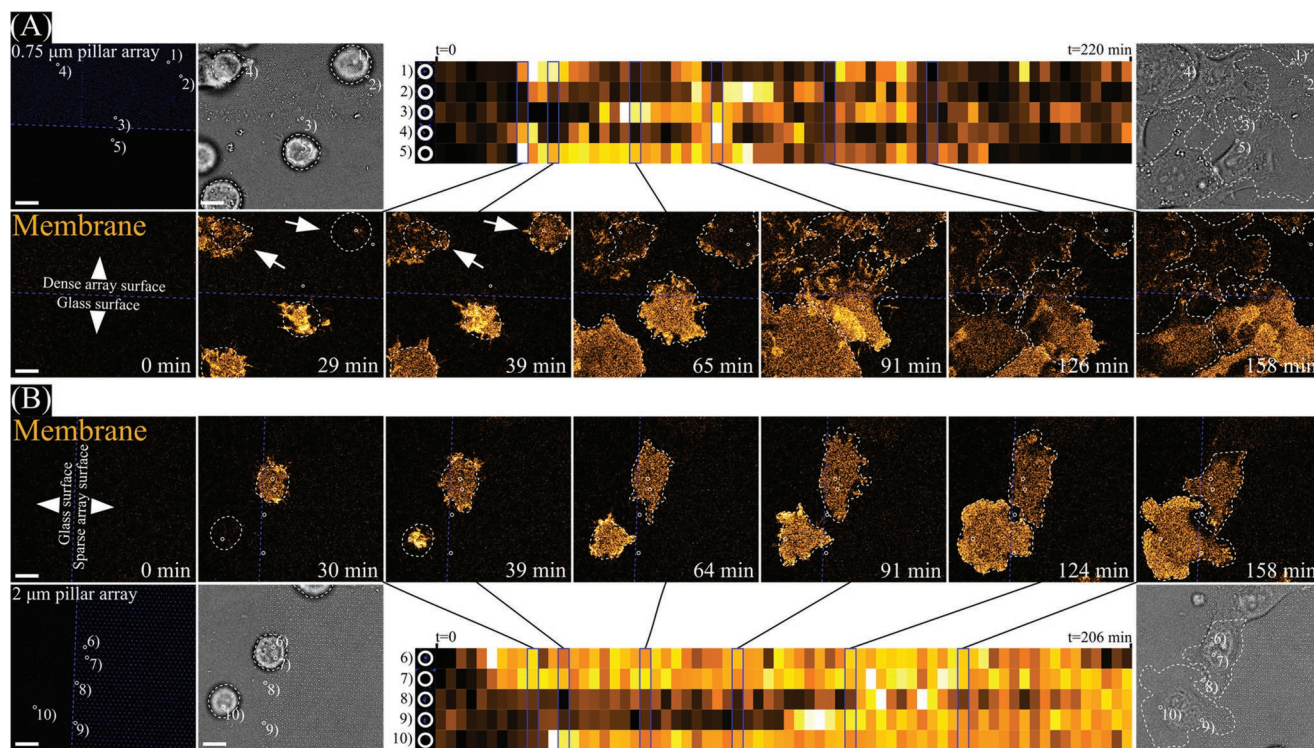


Figure 4. Confocal microscopy data recorded of NIH-3T3 fibroblasts expressing PH-PLC δ 1-mScarlet, localizing to the plasma membrane, settling onto dense (A, 0.75 μ m pitch) and sparse (B, 2 μ m pitch) nanopillar arrays. Images acquired at \approx 50% pillar height. Blue dashed lines indicate borders between glass surface and nanopillar arrays, white dashed lines indicate approximate cell shapes based on bright field images, white circles (1–10) indicate intensity traces of the membrane signal. On both dense and sparse arrays cells settling on the arrays initially contacted the glass coverslip (A: traces 1 and 4, and B: traces 6 and 7). Note the cells (white arrows) on the dense array after 29 min reaching down to the glass coverslip. On A) dense arrays the body of the cells subsequently pulled up and membrane signal was mainly observed toward the periphery of cells. This can be seen in traces 1, 2, and 4 where the membrane signal transiently increased for a few frames when the periphery of a cell moves across the nanopillar. On B) sparse arrays the membrane signal underneath the cell body was constant from the point of initial contact (traces 6 and 7). Cells on the glass surface showed stable membrane signal throughout (traces 5 and 10). Scale bars 10 μ m. Images presented are representative of $n \geq 100$ cells for both dense and sparse arrays.

For F-actin, we observe a highly dynamic situation, where the F-actin puncta are forming and disappearing at various locations in the cell as a function of time (see below for more detailed description of this process).

2.3. Fibroblast Migration

Once the initial adhesion and spreading has occurred, fibroblasts start migrating. We performed large scale migration experiments by time-lapse imaging of NIH-3T3 cells on at least four 2.25 mm² areas of each nanopillar array for up to 14 h 40 min. The fibroblasts were seeded 20 h prior to imaging.

Cell nuclei were labeled with a far-red fluorescent dye (SiR-DNA) and tracked (Figure 5A) using ImarisTrack (see the Experimental Section). Flower plots of trajectories from cells migrating on glass and 2 μm arrays are shown in Figure 5B,C. As small variations in cell seeding density, unavoidable between independent experiments, influence migration rates, data from two large scale migration experiments with similar cell density were analyzed separately, pooling together the data from individual sample wells recorded in parallel for each experiment (4 or 8 sample wells depending on the array). At the same time, the trends in the migration behavior were consistent between experiments. Figure 5D presents a brief summary of the cell migration data. For arrays with 2 μm pitch, migration data was

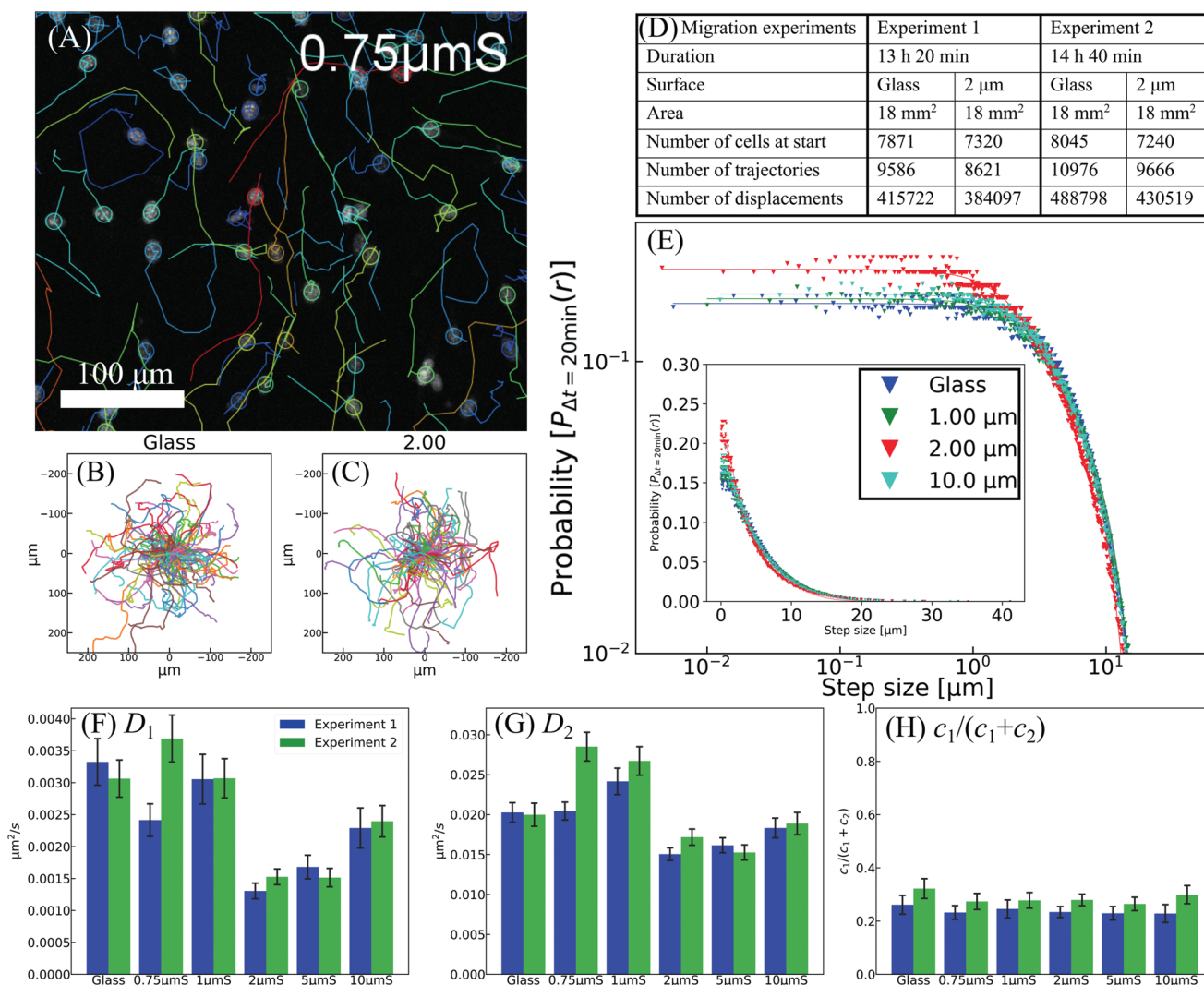


Figure 5. SiR-DNA-labeled nuclei of fibroblasts on nanopillar arrays and glass controls were imaged every 20 min and tracked for up to 14 h 40 min. A) Typical trajectories for tracked SiR-DNA stained nuclei in cells migrating on 0.75 μm pitch arrays. B,C) Representative sets of tracks are presented with a common origin. D) The surface area, number of cells, number of tracks, and displacements analyzed for cells migrating on glass and 2 μm pitch arrays are reported for the two presented experiments. For the four other pitch arrays (0.75, 1, 5, and 10 μm) these numbers were generally halved due to the design of the nanopillar samples. Glass and 2 μm pitch arrays were present on all samples, while samples either had 0.75 and 1 μm, or 5 and 10 μm pitch arrays in addition. The cell displacements were analyzed by constructing a probability distribution of step sizes (filled triangles, on a log–log and inset linear plot) and fitting to a double Gaussian model (solid lines) presented in (E). Fitted parameters D_1 , D_2 , and c_1 (weight coefficients depicted as $c_1/(c_1 + c_2)$) from the Gaussian model are presented in (F)–(H). Error bars are 95% confidence intervals for each parameter extracted from the least squares fitting of the double Gaussian model to the migration data.

recorded from a total area of 18 mm², a very large area considering the high resolution patterning technique. This area corresponds to 4.5×10^6 nanopillars for 2 μm arrays and to 32×10^6 nanopillars for 0.75 μm arrays.

Due to large variations in the migration rates for individual cells, cell trajectories were analyzed by a method proposed by Banigan et al.^[51] and described in detail in the Experimental Section. Briefly, for each data set, a probability density function of step sizes was generated and fitted to a double Gaussian model. In this model, the heterogeneously migrating cell population is modeled as the sum of two randomly migrating cell populations (one relatively immobile and one mobile population) with characteristic diffusion coefficients D_1 and D_2 as well as a weighting factors c_1 and c_2 for each population.

The resulting plots (Figure 5E) for Experiment 1, and determined values for diffusion coefficients for both experiments (Figure 5F,G) demonstrate that cell migration was inhibited on sparse nanopillar arrays compared to glass. Interestingly, the dependency on the nanopillar density was not directly proportional to nanopillar array pitch. On dense arrays (0.75–1 μm) cell migration was not significantly hampered, but on sparse arrays migration was strongly reduced, with migration recovering on 10 μm pitch. The slow population had a diffusion coefficient that was 7–10 times lower than the coefficient for the fast cell population on all substrates. The weighting factor, plotted as $c_1/(c_1 + c_2)$ in Figure 5H, reveals that about 25% of the analyzed displacements were modeled in the less mobile

D_1 population. Comparing with the glass control, migration on the 2 μm pitch substrates was reduced by 50% for the slow and 25% for the fast migrating cell population. Based on the confidence intervals not overlapping for data on glass and 2 μm pitch arrays, we can conclude that this difference is statistically significant with a p -value of at least $p = 0.05$.^[52,53]

2.4. High Resolution Investigation of Fibroblast Migration

To gain insight into the processes occurring during cell migration, especially the origin of observed migration rate differences, live-cell confocal imaging was performed on migrating fibroblasts expressing LifeAct-mNeonGreen and PH-PLCδ1-mScarlet. Selected time points from migrating fibroblasts on nanopillar arrays are shown in Figure 6. On dense nanopillar arrays, fast dynamics of densely spaced F-actin puncta were observed (see inserts in Figure 6A and Movies S04–S08 in the Supporting Information). Both F-actin and membrane signal were more intense close to cell periphery, indicating that the cells were close to the glass substrate in these regions and wrapped along the full length of the nanopillars. Only a weak enhancement of the membrane signal at the locations of nanopillars was observed (Figure 6B) for dense arrays. This indicates that small and dynamic membrane indentations where part of the plasma membrane was oriented parallel to the optical axis were formed for cells on these arrays. On sparse arrays the membrane signal was highly enhanced and stable (Figure 6D),

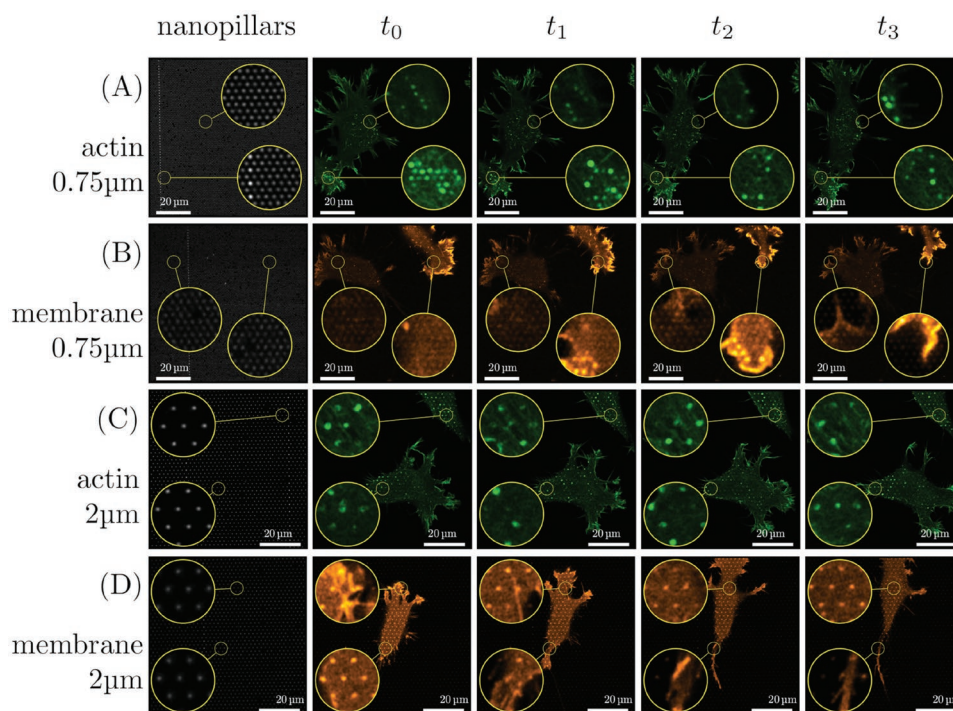


Figure 6. Migrating fibroblasts on nanopillar arrays. Sequence of images illustrating dynamical changes in F-actin and membrane configuration in cells migrating on dense and sparse nanopillar arrays. Circular insets show a magnified view of the same sample region for the image sequence in each row. A) Highly dynamical F-actin puncta were observed on dense arrays, while B) the signal originating from slight membrane indentations on the nanopillars was more stable. For sparse arrays, F-actin puncta associated with the nanopillars and could be observed as highly dynamic rings. D) Membrane signal on sparse arrays was constant and uniform for all nanopillars in contact with the cell. Time intervals A) 2.5 min B) 5 min, C) 5 min, and D) 10 min. Images presented are representative of $n \geq 50$ cells for both dense and sparse arrays.

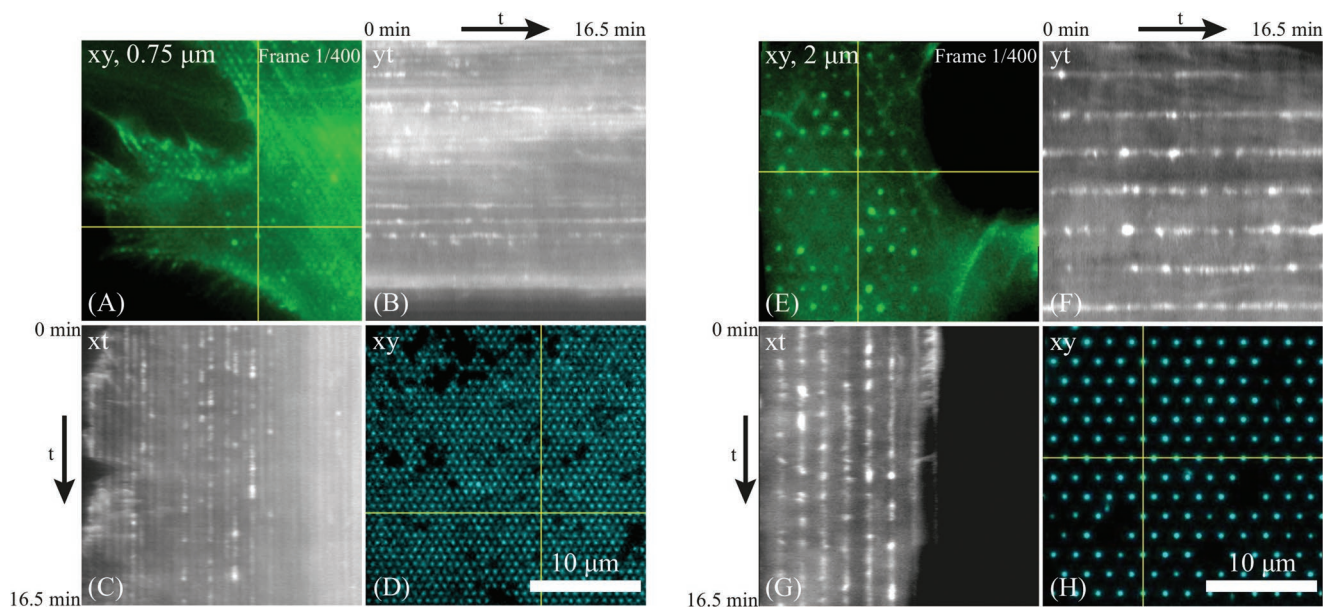


Figure 7. F-actin dynamics for NIH-3T3 fibroblasts expressing LifeAct-mNeonGreen recorded on A–C) dense and sparse E–G) nanopillar arrays. Gray scale images show xt and yt projections along the indicated lines in the xy plane images shown for A,E) $t = 0$ acquired at 2.5 s frame intervals. D,H) Corresponding nanopillar locations are shown. F-actin recruitment was transient on both dense and sparse arrays, but on the sparse arrays, F-actin was assembled for longer time periods and on a higher percentage of nanopillars. Also, the intensity of the F-actin signal recorded for the sparse array was higher. Images presented are representative of $n \geq 10$ cells for both dense and sparse arrays.

indicating that the cell membrane wraps along the full length of the nanopillars. The cell body maintained a stable contact with the glass support (see also Movies S09–S12 in the Supporting Information). On sparse arrays membrane at the trailing edge of the migrating cell appeared to remain associated with the nanopillars, which could be one reason for reduction in cell migration on sparse arrays. In contrast to the membrane signal (Figure 6D) which was uniform and stable, F-actin puncta seen in Figure 6C were highly dynamic. This highlights transient recruitment and disassembly of F-actin at nanopillar locations.

To gain a better insight into F-actin assembly/disassembly dynamics at nanopillars, time-lapses with increased frame rate were acquired by widefield microscopy. F-actin dynamics were visualized in xt and yt projections at nanopillar positions indicated by yellow lines on the xy image (Figure 7 and Movies S14–S16, Supporting Information). Actin recruitment was transient on both dense and sparse arrays, but on the sparse arrays, F-actin was assembled for longer time periods and on a higher percentage of nanopillars. This indicates that F-actin association could be caused by the membrane curvature at the nanopillars, which is increased on the sparse arrays due to cell wrapping the full length of the nanopillars.

Finally, focal adhesion dynamics were investigated during cell spreading and migration (Figure 8). On both dense and sparse arrays actin puncta colocalizing with nanopillars were observed 30 min after seeding, but focal adhesions had not yet formed. At 2 h, actin puncta were still visible on both densities, and small, round focal adhesions formed between the nanopillars at the cell periphery, especially on the sparser arrays. At 4 h, more elongated focal adhesions had formed on both sparse and dense arrays, and actin stress fibers were visible, especially on sparse arrays. Focal adhesions were formed mainly between

nanopillars, but some signal overlapped with nanopillars as well. To investigate focal adhesion dynamics during cell migration, time-lapse microscopy was performed of fibroblasts expressing talin-GFP. At the leading edge, new focal adhesions formed mainly between the nanopillars, although some adhesions also appeared to form around or in very close vicinity to nanopillars. At the trailing edge focal adhesion disadhesion and retraction into the cell body was observed, despite the presence of nanopillars, although the focal adhesion appeared to circumvent the nanopillars during retraction. Thus, focal adhesion driven adhesion likely serves mainly to anchor the cells to the substrate, while actin and membrane interactions occur on the nanopillars.

3. Discussion

Cell adhesion, spreading, and migration *in vitro* are highly studied processes, but studies have mainly been carried out on flat substrates such as glass, on gels or patterned surfaces. However, the geometry of the nanopillars introduce a new factor into the mechanobiology of cell adhesion and migration. To successfully maneuver the nanopillars, the main challenge for the cells appears to lie in shaping the plasma membrane to conform to the nanopillars. Theoretical models of cell adhesion and membrane conformation on nanopillar arrays emphasize the balance between membrane bending and surface adhesion.^[42,54,55]

Bending the cell membrane around each nanopillar requires energy to overcome the membrane bending stiffness, while adhesion to the surface of both the nanopillars and the substrate is energetically preferred for adherent cells used in

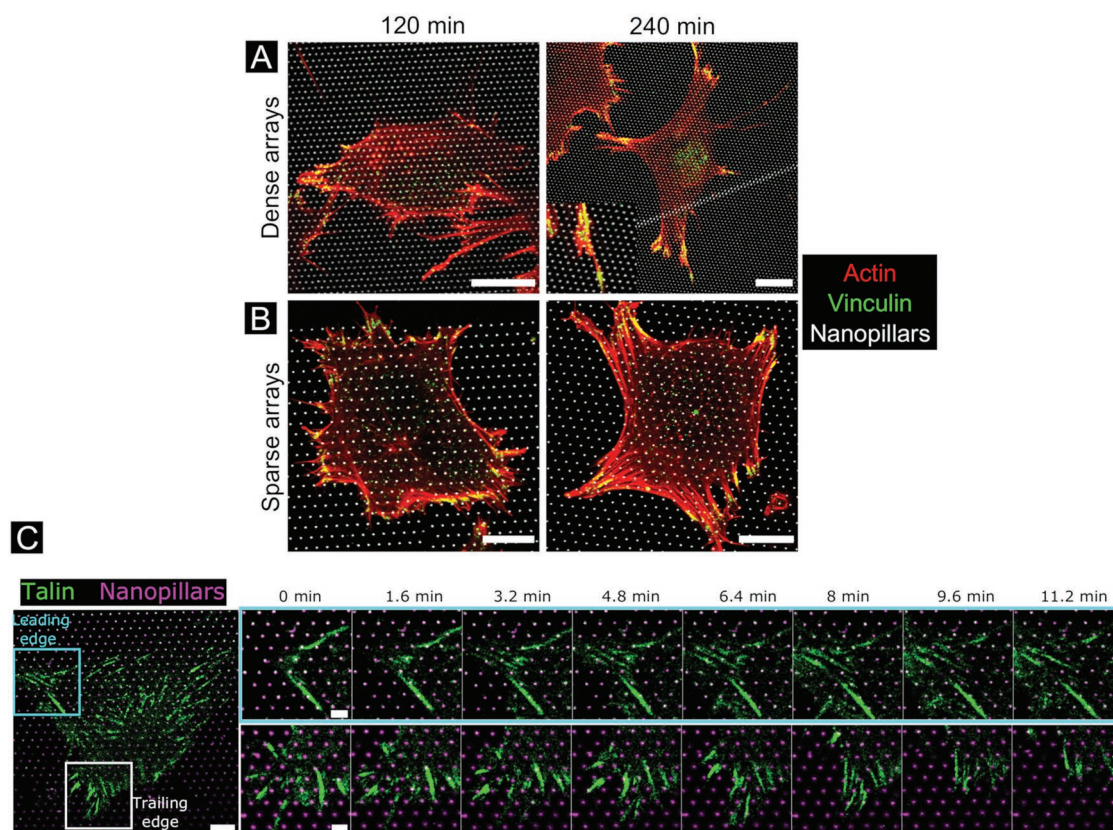


Figure 8. A,B) Actin and vinculin organization in spreading fibroblasts. Fibroblasts were seeded for 2 and 4 h before fixation and labeling of Phalloidin (Alexa488, red) and vinculin (Alexa555, green) on dense arrays (1 μm pitch) or sparse arrays (2 μm pitch). Yellow color indicates actin–vinculin overlap. All scale bars 10 μm. Images presented are representative of $n \geq 10$ cells for both dense and sparse arrays. C) Excerpts from a time-lapse of a fibroblast cell transduced with talin-GFP (green) on a 2 μm pitch nanopillar array (magenta), highlighting the formation of focal adhesions at the leading edge (cyan square) and trailing edge (white square) over a 11 min period. Scale bar 10 μm, excerpts 2 μm. Images presented are representative of $n \geq 5$ cells.

this study. Thus, on dense nanopillar array pitches, the cells adopt a suspended state while on sparser arrays the cells adopt a conformal state, engulfing the nanopillars and adhering to the substrate. In this work, these two states were observed for fully spread fibroblasts, with the transition occurring between 1 and 2 μm nanopillar array pitch. In addition, the detailed imaging performed here allowed several nuances to be observed.

During initial cell adhesion, nanopillar engulfment was observed regardless of nanopillar array pitch, which was not predicted in the theoretical models or observed experimentally before. The engulfment of the nanopillars likely has two interrelated contributing factors: membrane tension and actin polymerization forces. In general, depending on cell state and conformation, cells maintain significant membrane reserves stored as microscopic bends and buckles in the membrane.^[56,57] This could facilitate the initial engulfment of nanopillars regardless of array pitch. As the cell adhere and spread on the substrate, the membrane tension might increase, disfavoring nanopillar engulfment. Interestingly Pontes et al. recently reported that increased membrane tension acts as a mechanical signal triggering positioning of new rows of adhesions at the leading edge upon which cell migration velocity slows.^[58] This is in accordance with recent claims that the cell membrane functions as a long-range communication system

which can communicate and signal between distant parts of the cell to maintain cytoskeleton organization and polarity,^[59] challenging the traditional view where the membrane is regarded as a relatively passive scaffold for signaling.

The time-lapse and selected time-point observations performed here additionally resolved intermediate states. Even in cells on dense arrays fully spread after 24 h, small areas of cell membrane engulfing nanopillars were observed in cell peripheries. Likely, these protrusions are related to a separate factor involved in membrane dynamics. Membrane movement at the leading edge (especially in lamellipodia) is driven by actin polymerization, resulting in a substantial force on the membrane, and is combined with enhanced adhesive complex formation.^[60] These interrelated phenomena of actin polymerization and focal adhesion formation were observed in this work at the leading edge of migrating cells and around the cell periphery of spread and spreading cells on all nanopillar arrays. It appears that in our system, on array pitches down to 0.75 μm, actin polymerization and surface adhesions were sufficient to cause nanopillar engulfment at these locations, both initially, during cell adhesion and spreading, and later during cell migration. Once lamella replace lamellipodia, both actin polymerization and surface adhesion are diminished, resulting in suspension of the main cell body during spreading and migration on dense

arrays. On sparse arrays the adhesive forces appear to remain strong enough to counter the increasing membrane tension, resulting in an adhered, nanopillar-engulfing state both during initial spreading and migration.

The distinction between these states has a strong influence on cell migration rates. Previous work with silicon nanowires and nanopillars has indeed shown strong reduction of migration in the sparse array regime, while less of a reduction was observed on dense arrays.^[30,31,61,62] The mechanisms for reduction of cell migration on sparse arrays are attributed to cytoskeletal and membrane entanglement by the nanostructures. Our results support these general descriptions, as in the sparse array regime both membrane engulfment and strong dynamic F-actin puncta association were observed. The requirement of continuous reorganization of the membrane and cytoskeleton in response to the moving cell likely causes a significant reduction of migration rates. A further effect of the nanopillars was observed where membrane residues were left behind on the nanopillars during retraction of the trailing edge. This indicates a strong adhesion between the membrane and nanopillars, so strong that the membrane does not release, but remains bound and forms membrane tethers at nanopillars. Strong membrane adhesion of cells to silicon nanowires has been reported,^[33] and extraction of membrane tethers is a well-known method of assessing membrane tension of cells.^[63] Such tethers are produced when an outward force is applied to a small area of the cell membrane and requires the loss of association between the cytoskeleton and cell membrane. Thus, the membrane binding and tether extraction at the trailing edge of migrating cells act as a further hindrance for cell migration.

There are several opportunities for further investigations of cell migration on this platform. The exact mechanism of recruitment and function of the F-actin puncta or bundles around the nanopillars are not known. Using superresolution imaging we have previously shown that in HeLa cells these puncta are in fact rings or cylinders formed around the nanopillars.^[32] In a recent report by Hanson et al., similar puncta and rings were observed and attributed to cell adhesion to nanopillars.^[40] As F-actin puncta were observed to be highly dynamic in this work, disappearing and appearing over a few minutes, it does not seem likely that these F-actin puncta are solely involved in adhesion. Especially, as membrane engulfment of nanopillars was generally observed both with and without F-actin enrichment at the nanopillar site, this is not a continuous requirement for cell adhesion to nanopillars. We consider it likely that the dynamic F-actin enrichments are involved in the reorganization of the cell membrane as the cells migrate on nanopillar arrays, in addition to adherence processes. In a recent study, Daste et al. showed that membrane curvature induced by using liposomes with various sizes, combined with PI(4,5)P₂, and PI(3)P signaling, are needed to trigger actin polarization.^[64] Some actin assemblies induced by membrane curvature on the sparse arrays (see Movie S15 in the Supporting Information) resembled actin comets induced in the cell-free assay employed by Daste et al. Similar interactions with the cytoskeleton have also been recently reported for silicon nanoneedle arrays.^[23]

The role of nanopillar surface chemistry also remains to be investigated. Although geometry was attributed the leading role in reduced neuronal migration on nanopillars (Si, SiO₂, and Pt

were tested),^[31] it cannot be ruled out that the surface chemistry of SU-8 could play a role in the strong membrane interactions observed, and should be investigated further.

4. Conclusion

High resolution live cell imaging together with imaging of fixed cells and cell migration statistics reveal that nanopillars strongly influence both the quantitative and qualitative properties of fibroblast migration. From a fundamental perspective these results highlight the strong influence surface topography can have on cell function, inducing, e.g., novel regimes of cell motility. From an applications perspective, the results demonstrate how important it is to investigate dynamic effects, as these reveal a nanostructure-cell interaction that changes both over time and even in different locations of the cell. The detailed interactions demonstrated here can have important implications for applications such as in vivo biointerfaces with nanowires or nanopillars, advanced in vitro applications such as neuronal guidance and network construction, stem cell differentiation, and mechanobiology.

5. Experimental Section

Nanopillar Fabrication: All chemicals and reagents were purchased from Sigma-Aldrich (Oslo, Norway) unless otherwise specified. SU-8 nanopillar arrays on glass were prepared as previously described.^[32] Briefly, 1 μm thick SU-8 films were spin coated on 0.17 mm (#1.5) glass cover slips (Menzel-Gläser borosilicate glass) and soft-baked for 1 min. Fluorescent SU-8 was made by including Oxazine-170 in the SU-8 solution (100 μm mL⁻¹). Nanopillars were defined using an Elionix GLS-100 EBL-system. Samples were post-exposure baked for 3 min and developed for 40 s using mr-Dev 600 (Microchem, USA). The resulting nanopillars were 1 μm high and had tip diameters in the range of 90 nm. All samples were treated with oxygen plasma before use.

Cell Migration: NIH-3T3 cells (a kind gift from T. Sandal, NTNU) were maintained in Dulbecco's modified Eagle medium (DMEM) with 10% fetal bovine serum (FBS), 1% pen/strep, 1% non-essential amino acids for minimum essential medium (MEM), 0.5% L-glutamine at 37 °C. Seeding density was typically 25 000–30 000 cells cm⁻². Twenty to twenty-four hours after cell seeding and 30–60 min before commencing imaging, the far-red fluorescent dye silicon rhodamine SiR-DNA dye (Spirochrome) was added to the cell medium at a concentration of 1 μM. The cells were kept in the medium together with SiR-DNA for the duration of the migration experiment. Cells were imaged at 37 °C with 5% CO₂ using a 10× objective in an EVOS FL Auto 2 microscope. Cells were cultured on 3 × 3 mm nanopillar arrays, containing four 1.5 × 1.5 mm² areas with either 0.75, 1, 2 μm pitch and glass control, or 2, 5, 10 μm pitch and glass control. Images were recorded with 20 min intervals (Δt = 1200 s) for up to 14 h 40 min. In each experiment four wells containing the dense arrays and four wells containing sparse arrays were imaged simultaneously. Nuclei positions were identified and tracked using the Imaris application ImarisTrack (Bitplane). From each experiment ≈5000 cell trajectories were analyzed for 0.75, 1, 5, and 10 μm pitch and ≈9000–11 000 tracks for 2 μm pitch, giving a total of about 200 000 and 450 000 cell displacements, respectively. Probability density functions of cell displacements were analyzed and fit to a double Gaussian function as described by Banigan et al.^[51] Probability density function of cell displacements was constructed by assigning a chosen number of displacements *m* to each bin (*m* = 700 was chosen by Banigan et al.^[51] and was used in this work as well). The position of each bin was the average step size of that bin, while each bin was assigned a weight $W_i = 1/(r_{max}^i - r_{min}^i)$, where r_{max}^i and r_{min}^i were the maximum and

minimum displacements in that bin. This gives a normalized probability density function (which in our case summed to 2, as absolute values of all displacements were used). Note that we also pooled all x and y displacements. This probability density function was then fit to a double Gaussian of the form

$$G_{\Delta t}(r) = \frac{c_1}{\sqrt{4\pi D_1 \Delta t}} e^{-\frac{r^2}{4\pi D_1 \Delta t}} + \frac{c_2}{\sqrt{4\pi D_2 \Delta t}} e^{-\frac{r^2}{4\pi D_2 \Delta t}} \quad (1)$$

where $c_1 + c_2 = 2$ are the population weighting coefficients, D_1 and D_2 are the characteristic diffusion coefficient for each population, r is the cell displacement distance, and Δt is the used frame rate. The double Gaussian was fit to the probability density functions for each sample using least squares fitting, and 95% confidence intervals for each parameter were extracted as error estimates. Data was analyzed using custom Python scripts and the Imfit-py package for fitting.^[65]

High Resolution Cell Imaging and Immunofluorescence: Gateway cloning (ThermoFisher) was used to generate lentiviral expression vectors for transducing NIH-3T3 cells. The PH domain from human PLCd1, LifeAct, and mScarlet (all synthetic GeneArt Strings, ThermoFisher), and mNeonGreen (Allele Biotech) were cloned into Gateway pEntry vectors. All entry constructs were verified by Sanger sequencing (GATC Biotech) before further use. PuroR in pLex307 was replaced with BlastR to generate Gateway lentiviral destination vectors with corresponding antibiotic resistances. 2-Fragment Gateway recombination with pLex307 or pLex307-Blast was performed to generate LifeAct-mNeonGreen and PH-PLCd1-mScarlet constructs in lentiviral delivery vectors. Lentiviral production was performed in HEK293T cells as described^[66] using 3rd generation packaging system with pMDL.g/pRRE, pMD2.G, and pRSV-Rev (all from Addgene) and JetPrime (PolyPlus) as transfection reagent. Virus-containing supernatant was harvested 2 and 3 days post transfection and NIH-3T3 cells were transduced in the supernatant in the presence of polybrene (8 $\mu\text{g mL}^{-1}$), and selected in puromycin (1 $\mu\text{g mL}^{-1}$) and blasticidine (10 $\mu\text{g mL}^{-1}$) for 1 week.; Cell imaging commenced 0–24 h after seeding, or during seeding after trypsination, and was done at 37 °C and 5% CO₂ with Zeiss LSM 800 Airyscan (Axiovert 200M inverted) CLS-microscope with a C-Apochromat 63 \times /1.15 W objective (Figure 6) or Zeiss LSM 880 Airyscan AxioObserver with a LD LCI Plan-Apochromat 40 \times /1.2W objective (Figure 2 C–F) or Leica TCS SP8 HC PL APO CS2 63 \times /1.20W objective (Figures 2 A–C and 4) or Zeiss Laser TIRF 3 with an alpha Plan-Apochromat 100 \times /1.46 oil objective in both EPI fluorescence and TIRF mode (Figures 3 and 7). NIH-3T3 cells were also transduced with BacMam 2.0 CellLights Talin-GFP (ThermoFisher) targeting focal adhesion and imaged at 37 °C in Leibovitz's L-15 Medium using a 63 \times 1.4 oil objective on a Leica SP8 microscope (Figure 8 C). Cells were prepared for immunofluorescence using a protocol described by Whelan et al.^[67] with some modifications. Briefly, cells were fixed in 4% paraformaldehyde (PFA) for 2.5 min with no prior rinsing, washed in PBS, permeabilized in 0.1% triton X-100 in PBS for 5 min, washed, blocked in 1% BSA in PBS for 15 min, incubated with antivinculin (1:200) for 1 h, washed, incubated with Alexa555 secondary antibody (1:500) for 1 h, washed, and finally incubated with Alexa488-phalloidin for 30 min. Fixed cells were imaged in PBS using a 63 \times 1.4 oil objective on a Leica SP8 microscope (Figure 8A,B) with system-optimized voxel sizes (typically 70 nm in xy).

Supporting Information

Supporting Information is available from the Wiley Online Library or from the author.

Acknowledgements

K.S.B. and S.U. contributed equally to this work. The authors would like to acknowledge Rasmus Schanke for initial experiments. The Research

Council of Norway is acknowledged for the support to the Norwegian Micro- and Nano-Fabrication Facility (NorFab, grant number 245963/F50). NTNU is acknowledged for the financial support for J.V. through Nano@NTNU enabling technologies program and S.U. through NTNU Biotechnology enabling technologies program. This work was also partly supported by the Research Council of Norway through its Centres of Excellence funding scheme, project number 223255/F50.

Conflict of Interest

The authors declare no conflict of interest.

Keywords

cell migration, nanofabrication, nanopillars, SU-8

Received: May 16, 2019

Revised: July 25, 2019

Published online: August 29, 2019

- [1] A. F. McGuire, F. Santoro, B. Cui, *Annu. Rev. Anal. Chem.* **2018**, *11*, 101.
- [2] T. E. McKnight, A. V. Melechko, D. K. Hensley, D. G. J. Mann, G. D. Griffin, M. L. Simpson, *Nano Lett.* **2004**, *4*, 1213.
- [3] W. Kim, J. K. Ng, M. E. Kunitake, B. R. Conklin, P. Yang, *J. Am. Chem. Soc.* **2007**, *129*, 7228.
- [4] W. Hällström, T. Mårtensson, C. Prinz, P. Gustavsson, L. Montelius, L. Samuelson, M. Kanje, *Nano Lett.* **2007**, *7*, 2960.
- [5] J. J. VanDersarl, A. M. Xu, N. A. Melosh, *Nano Lett.* **2012**, *12*, 3881.
- [6] J. Pan, Z. Lyu, W. Jiang, H. Wang, Q. Liu, M. Tan, L. Yuan, H. Chen, *ACS Appl. Mater. Interfaces* **2014**, *6*, 14391.
- [7] J. Peng, M. A. Garcia, J.-S. Choi, L. Zhao, K.-J. Chen, J. R. Bernstein, P. Peyda, Y.-S. Hsiao, K. W. Liu, W.-Y. Lin, A. D. Pyle, H. Wang, S. Hou, H.-R. Tseng, *ACS Nano* **2014**, *8*, 4621.
- [8] Y. Wang, Y. Yang, L. Yan, S. Y. Kwok, W. Li, Z. Wang, X. Zhu, G. Zhu, W. Zhang, X. Chen, P. Shi, *Nat. Commun.* **2014**, *5*, 4466.
- [9] C. Chiappini, J. O. Martinez, E. De Rosa, C. S. Almeida, E. Tasciotti, M. M. Stevens, *ACS Nano* **2015**, *9*, 5500.
- [10] J. T. Robinson, M. Jorgolli, A. K. Shalek, M.-H. Yoon, R. S. Gertner, H. Park, *Nat. Nanotechnol.* **2012**, *7*, 180.
- [11] Z. Yu, T. E. McKnight, M. N. Ericson, A. V. Melechko, M. L. Simpson, B. Morrison, *Nano Lett.* **2007**, *7*, 2188.
- [12] C. Xie, Z. Lin, L. Hanson, Y. Cui, B. Cui, *Nat. Nanotechnol.* **2012**, *7*, 185.
- [13] S. Wang, Y. Wan, Y. Liu, *Nanoscale* **2014**, *6*, 12482.
- [14] H. J. Yoon, M. Kozminsky, S. Nagrath, *ACS Nano* **2014**, *8*, 1995.
- [15] S.-K. Lee, G.-S. Kim, Y. Wu, D.-J. Kim, Y. Lu, M. Kwak, L. Han, J.-H. Hyung, J.-K. Seol, C. Sander, A. Gonzalez, J. Li, R. Fan, *Nano Lett.* **2012**, *12*, 2697.
- [16] M. A. Bucaro, Y. Vasquez, B. D. Hatton, J. Aizenberg, *ACS Nano* **2012**, *6*, 6222.
- [17] V. Errico, G. Arrabito, E. Fornetti, C. Fuoco, S. Testa, G. Saggio, S. Rufini, S. Cannata, A. Desideri, C. Falconi, C. Gargioli, *ACS Appl. Mater. Interfaces* **2018**, *10*, 14097.
- [18] Y.-R. Na, S. Y. Kim, J. T. Gaublomme, A. K. Shalek, M. Jorgolli, H. Park, E. G. Yang, *Nano Lett.* **2013**, *13*, 153.
- [19] C. Chiappini, *ACS Sensors* **2017**, *2*, 1086.
- [20] C. Chiappini, P. Campagnolo, C. S. Almeida, N. Abbassi-Ghadi, L. W. Chow, G. B. Hanna, M. M. Stevens, *Adv. Mater.* **2015**, *27*, 5147.

- [21] C. Xie, L. Hanson, Y. Cui, B. Cui, *Proc. Natl. Acad. Sci. USA* **2011**, *108*, 3894.
- [22] A. Dmitriev, C. Häggglund, S. Chen, H. Fredriksson, T. Pakizeh, M. Käll, D. S. Sutherland, *Nano Lett.* **2008**, *8*, 3893.
- [23] C. S. Hansel, S. W. Crowder, S. Cooper, S. Gopal, M. João Pardelha da Cruz, L. de Oliveira Martins, D. Keller, S. Rothery, M. Becce, A. E. G. Cass, C. Bakal, C. Chiappini, M. M. Stevens, *ACS Nano* **2019**, *13*, 2913.
- [24] H. Amin, M. Dipalo, F. De Angelis, L. Berdondini, *ACS Appl. Mater. Interfaces* **2018**, *10*, 15207.
- [25] J.-Y. Shiu, L. Aires, Z. Lin, V. Vogel, *Nat. Cell Biol.* **2018**, *20*, 262.
- [26] P. Paulitschke, F. Keber, A. Lebedev, J. Stephan, H. Lorenz, S. Hasselmann, D. Heinrich, E. M. Weig, *Nano Lett.* **2019**, *19*, 2207.
- [27] J. Seo, J. Kim, S. Joo, J. Y. Choi, K. Kang, W. K. Cho, I. S. Choi, *Small* **2018**, *14*, 1801763.
- [28] J. Tang, N. Qin, Y. Chong, Y. Diao, Yiliguma, Z. Wang, T. Xue, M. Jiang, J. Zhang, G. Zheng, *Nat. Commun.* **2018**, *9*, 786.
- [29] S. Bonde, N. Buch-Månson, K. R. Rostgaard, T. K. Andersen, T. Berthing, K. L. Martinez, *Nanotechnology* **2014**, *25*, 362001.
- [30] H. Persson, C. Købler, K. Mølhave, L. Samuelson, J. O. Tegenfeldt, S. Oredsson, C. N. Prinz, *Small* **2013**, *9*, 4006.
- [31] C. Xie, L. Hanson, W. Xie, Z. Lin, B. Cui, Y. Cui, *Nano Lett.* **2010**, *10*, 4020.
- [32] K. S. Beckwith, S. P. Cooil, J. W. Wells, P. Sikorski, *Nanoscale* **2015**, *7*, 8438.
- [33] S. Qi, C. Yi, S. Ji, C.-C. Fong, M. Yang, *ACS Appl. Mater. Interfaces* **2009**, *1*, 30.
- [34] A. SanMartin, F. Johansson, L. Samuelson, C. N. Prinz, *J. Nanosci. Nanotechnol.* **2014**, *14*, 4880.
- [35] M. Dipalo, A. F. McGuire, H.-Y. Lou, V. Caprettini, G. Melle, G. Bruno, C. Lubrano, L. Matino, X. Li, F. De Angelis, B. Cui, F. Santoro, *Nano Lett.* **2018**, *18*, 6100.
- [36] F. Mumm, K. M. Beckwith, S. Bonde, K. L. Martinez, P. Sikorski, *Small* **2013**, *9*, 263.
- [37] T. Berthing, S. Bonde, K. R. Rostgaard, M. H. Madsen, C. B. Sørensen, J. Nygård, K. L. Martinez, *Nanotechnology* **2012**, *23*, 415102.
- [38] W. Zhao, L. Hanson, H.-Y. Lou, M. Akamatsu, P. D. Chowdary, F. Santoro, J. R. Marks, A. Grassart, D. G. Drubin, Y. Cui, B. Cui, *Nat. Nanotechnol.* **2017**, *12*, 750.
- [39] H.-Y. Lou, W. Zhao, Y. Zeng, B. Cui, *Acc. Chem. Res.* **2018**, *51*, 1046.
- [40] L. Hanson, W. Zhao, H.-Y. Lou, Z. C. Lin, S. W. Lee, P. Chowdary, Y. Cui, B. Cui, *Nat. Nanotechnol.* **2015**, *10*, 554.
- [41] S. Bonde, T. Berthing, M. H. Madsen, T. K. Andersen, N. Buch-Månson, L. Guo, X. Li, F. Badique, K. Anselme, J. Nygård, K. L. Martinez, *ACS Appl. Mater. Interfaces* **2013**, *5*, 10510.
- [42] N. Buch-Månson, S. Bonde, J. Bolinsson, T. Berthing, J. Nygård, K. L. Martinez, *Adv. Funct. Mater.* **2015**, *25*, 3246.
- [43] J. Riedl, A. H. Crevenna, K. Kessenbrock, J. H. Yu, D. Neukirchen, M. Bista, F. Bradke, D. Jenne, T. A. Holak, Z. Werb, M. Sixt, R. Wedlich-Soldner, *Nat. Methods* **2008**, *5*, 605.
- [44] D. S. Bindels, L. Haarbosch, L. van Weeren, M. Postma, K. E. Wiese, M. Mastop, S. Aumonier, G. Gotthard, A. Royant, M. A. Hink, T. W. J. Gadella, *Nat. Methods* **2017**, *14*, 53.
- [45] M. A. Lemmon, K. M. Ferguson, R. O'Brien, P. B. Sigler, J. Schlessinger, *Proc. Natl. Acad. Sci. USA* **1995**, *92*, 10472.
- [46] T. Svitkina, *Cold Spring Harb. Perspect. Biol.* **2018**, *10*, a018267.
- [47] H. Huxley, *J. Mol. Biol.* **1963**, *7*, 281.
- [48] D. T. Woodrum, *J. Cell Biol.* **1975**, *67*, 231.
- [49] H. Lorenz, M. Despont, N. Fahrni, J. Brugger, P. Vettiger, P. Renaud, *Sens. Actuators, A* **1998**, *64*, 33.
- [50] K. V. Nemani, K. L. Moodie, J. B. Brennick, A. Su, B. Gimi, *Mater. Sci. Eng. C* **2013**, *33*, 4453.
- [51] E. J. Banigan, T. H. Harris, D. A. Christian, C. A. Hunter, A. J. Liu, *PLOS Comput. Biol.* **2015**, *11*, e1004058.
- [52] S. A. Julious, *Pharm. Stat.* **2004**, *3*, 217.
- [53] P. C. Austin, J. E. Hux, *J. Vasc. Surg.* **2002**, *36*, 194.
- [54] P. Verma, I. Y. Wong, N. A. Melosh, *Biointerphases* **2010**, *5*, 37.
- [55] X. Xie, A. M. Xu, M. R. Angle, N. Tayebi, P. Verma, N. A. Melosh, *Nano Lett.* **2013**, *13*, 6002.
- [56] N. Groulx, F. Boudreault, S. N. Orlov, R. Grygorczyk, *J. Membr. Biol.* **2006**, *214*, 43.
- [57] L. Figard, A. M. Sokac, *Bioarchitecture* **2014**, *4*, 39.
- [58] B. Pontes, P. Monzo, L. Gole, A.-L. Le Roux, A. J. Kosmalka, Z. Y. Tam, W. Luo, S. Kan, V. Viasnoff, P. Roca-Cusachs, L. Tucker-Kellogg, N. C. Gauthier, *J. Cell Biol.* **2017**, *216*, 2959.
- [59] P. Sens, J. Plastino, *J. Phys.: Condens. Matter* **2015**, *27*, 273103.
- [60] A. Huttenlocher, A. R. Horwitz, *Cold Spring Harb. Perspect. Biol.* **2011**, *3*, a005074.
- [61] H. Persson, Z. Li, J. O. Tegenfeldt, S. Oredsson, C. N. Prinz, *Sci. Rep.* **2015**, *5*, 18535.
- [62] N. Buch-Månson, D.-H. Kang, D. Kim, K. E. Lee, M.-H. Yoon, K. L. Martinez, *Nanoscale* **2017**, *9*, 5517.
- [63] R. Dimova, *Adv. Colloid Interface Sci.* **2014**, *208*, 225.
- [64] F. Daste, A. Walrant, M. R. Holst, J. R. Gadsby, J. Mason, J.-E. Lee, D. Brook, M. Mettlen, E. Larsson, S. F. Lee, R. Lundmark, J. L. Gallop, *J. Cell Biol.* **2017**, *216*, 3745.
- [65] M. Newville, T. Stensitzki, D. B. Allen, A. Ingargiola **2014**, <https://doi.org/10.5281/zenodo.11813>.
- [66] G. Tiscornia, O. Singer, I. M. Verma, *Nat. Protoc.* **2006**, *1*, 241.
- [67] D. R. Whelan, T. D. M. Bell, *Sci. Rep.* **2015**, *5*, 7924.